A Series Arc Fault Detection Method Based on Time-Frequency Markov Permutation Transition Field for Photovoltaic Systems With Power Electronic Devices

Zhendong Yin, Shuang Peng, Chunyu Xiao, Li Wang, *Member, IEEE*, and Shanshui Yang

***Abstract*—Series arc faults (SAFs) are a primary cause of fire incidents in photovoltaic systems. Accurately and rapidly detecting SAF under the interference of power electronic devices remains a significant challenge. This article proposes an SAF detection method based on the time-frequency Markov permutation transition field (TFMPTF). First, variational mode decomposition is used to decompose the current signal into modes containing different frequency components to prevent interference between the information of different frequency bands. Then, the modes are transformed into two-dimensional matrices using TFMPTF. Innovatively, the concept of time-frequency permutation patterns state transition analysis in TFMPTF is proposed, from which the distinct structural information of the current signal can be effectively depicted. Afterward, singular value decomposition is employed to extract fault features from matrices. Finally, fault features are processed using a kernel extreme learning machine to obtain detection results. Offline experimental results show that the average detection accuracy of the proposed method is 98.97%, and the advancedness and adaptability of the proposed method are verified by comparing it with different methods. The proposed method and comparison methods are implemented in a microprogrammed control unit (MCU) for online experiments, further confirming that the detection speed and detection accuracy of the proposed method are reliable.**

***Index Terms*—Arc fault, kernel extreme learning machine (KELM), Markov transition matrix, photovoltaic (PV) system, variational mode decomposition (VMD).**

Acronyms

SAF	Series arc fault.
PV	Photovoltaic.
TFMPTF	Time-frequency Markov permutation transition field.
VMD	Variational mode decomposition.
SVD	Singular value decomposition.
KELM	Kernel extreme learning machine.
MCU	Microprogrammed control unit.
MPPT	Maximum power point tracking.
NEC	National Electrical Code.
SVM	Support vector machine.
RF	Random forests.
RP	Recurrence plots.
IRP	Improved recurrence plots.
RQA	Recurrence quantification analysis.
MTF	Markov transition field.
TMPTM	Time Markov permutation transition matrix.
FMPTM	Frequency Markov permutation transition matrix.
ELM	Extreme learning machine.
PSO	Particle swarm optimization.
DAQ	Data acquisition.
PMSM	Permanent magnet synchronous motor.
PF	Proposed feature extraction method.
Std	Standard deviation.
Var	Variance.
PUF	Pulse factor.
KF	Kurtosis factor.
WTEnt	Wavelet energy entropy.
MFE	Multiscale fuzzy entropy.
EMD	Empirical mode decomposition.
FDE	Frequency domain energy.
MMV	Min-to-max value.
PCA	Principal component analysis.
LDA	Linear discriminant analysis.
NNMF	Non-negative matrix factorization.
ABT	AdaBoost.
GRBT	GradientBoosting.
HiGRBT	HistGradientBoosting.
ET	Extra trees.
NN	Neural network.
EHCNN	Enhanced convolutional neural network.

Received 19 October 2024; revised 14 January 2025 and 24 February 2025; accepted 25 March 2025. Date of publication 28 March 2025; date of current version 26 May 2025. This work was supported by the National Natural Science Foundation of China under Grant 51877102. Recommended for publication by Associate Editor J. Lam. *(Corresponding author: Shanshui Yang.)*

Zhendong Yin, Shuang Peng, and Chunyu Xiao are with the College of Electrical, Energy and Power Engineering, Yangzhou University, Yangzhou 225127, China (e-mail: zdyin@yzu.edu.cn; MX120230683@stu.yzu.edu.cn; MZ120231206@stu.yzu.edu.cn).

Li Wang and Shanshui Yang are with the Department of Electrical Engineering, College of Automation, Nanjing University of Aeronautics and Astronautics, Nanjing 210000, China (e-mail: liwang@nuaa.edu.cn; yshanshui@nuaa.edu.cn).

Color versions of one or more figures in this article are available at https://doi.org/10.1109/TPEL.2025.3555829.

Digital Object Identifier 10.1109/TPEL.2025.3555829

I. Introduction

THE excessive consumption of traditional fossil fuels has exacerbated environmental pollution and the global

greenhouse effect. Therefore, it is essential to vigorously develop new alternative energy sources. Photovoltaic (PV) energy has the advantages of abundant reserves, cleanliness, and no geographical restrictions. In theory, PV energy can satisfy the energy needs of all countries [1]. In 2023, the global PV system installation capacity reached 444 GW, and PV energy is playing an increasingly critical role in this world. However, the safety of PV systems is highly susceptible to dc arc faults during long-term operation [2]. DC arc faults represent a type of plasma discharge phenomenon that can penetrate the air. The temperature at the site of a dc arc fault may reach as high as 3000°C, which can easily ignite nearby combustible materials and potentially lead to fires within the system. DC arc faults can be regarded as introducing stochastic impedance into the circuit, which complicates the inverter's ability to accurately perform maximum power point tracking (MPPT) and subsequently diminishes the efficiency of the PV system. Consequently, dc arc faults pose a significant threat to the safety of PV systems, making it imperative to detect them promptly in order to ensure system safety. The National Electrical Code (NEC) states that PV systems with voltage levels above 80 V must possess arc fault detection capabilities [3]. Compared to dc parallel arc faults, dc series arc faults (SAFs) pose a greater hazard to PV systems [4]. The arc-like noise generated by the power electronic devices in PV systems poses a significant challenge to accurately detect SAF.

Scholars have proposed SAF detection methods based on physical phenomena, such as sound, light, and electromagnetic radiation. However, these methods are only applicable to scenarios with limited space. The SAF detection methods based on current signals are not limited by the size of the application scenario and are the main means of detecting SAF at present.

By extracting the average value of the spectral energy of the arc current within the range of 48.83 to 93.99 kHz, it is possible to determine whether an arc fault occurred [5]. In [6], SAF detection was achieved by extracting the reflection waveform amplitude based on spread spectrum time domain reflectometry. Some scholars measured the uncertainty information of arc current by extracting Tsallis entropy [7] and Hurst index [8], with which normal condition and SAF condition can be distinguished. The abovementioned methods implement SAF detection by setting a threshold, however, detection methods based on a single threshold are difficult to effectively adapt to the complex operation states of the systems [9].

Currently, scholars have integrated different types of arc features based on machine learning algorithms to enhance the adaptability of SAF detection methods. Machine learning algorithms are capable of adaptively uncovering the intricate nonlinear relationships between fault features and fault classifications [10]. In [11], different types of features (variance, pulse factor, kurtosis factor, and wavelet energy entropy) were fused based on the extreme learning machine (ELM) to obtain the detection results. The randomness of arc current under different scales can be measured by extracting the multiscale fuzzy entropy from the components obtained based on variational mode decomposition (VMD) [12], and a support vector machine (SVM) was utilized to achieve SAF detection. In [13], the complete ensemble empirical mode decomposition (EMD) with the adaptive noise was utilized to decompose the current signal, and the fusion of 16-dimensional feature vectors was achieved based on SVM. In [14], five features reflecting the time-domain fluctuation characteristics of the current signal were input into the random forests (RF) to obtain the probability of an SAF occurring. Inputting the original one-dimensional arc current into a deep convolutional neural network can directly extract abstract fault features [15]. The fusion of different types of fault information in one-dimensional current signals based on a machine-learning algorithm can enhance the adaptability of the detection method.

However, compared with the original one-dimensional signals, the converted two-dimensional matrixes can possess more distinct structural information and spatial correlation information between data points [16], [17], from which it is more conducive to extracting subtle internal features [18]. Nowadays, the fault diagnosis method based on converting one-dimensional signals into two-dimensional matrices is receiving increasing attention [19].

In [20] and [21], wavelet transform (WT) is utilized to decompose the arc current into multiple one-dimensional components, which are then used to construct a two-dimensional matrix, and SAF detection is achieved by mining the texture information from this matrix. In [22], the current signal is processed using fractional Fourier transform, from which a two-dimensional time-frequency matrix can be obtained, and then the singular values extracted from the two-dimensional time-frequency matrix are fused based on SVM. The two-dimensional matrix obtained from recurrence plots (RP) contains crucial chaotic information about the arc current [23], and the DET of two-dimensional matrix can differentiate between normal conditions and SAF conditions. To overcome the shortcoming that traditional RP can easily lose high-frequency fault information, improved RP (IRP) is proposed in [24], and recurrence quantification analysis (RQA) based features and singular values are extracted from two-dimensional matrix for SAF detection. In [25], the reconstruction of the attractor track is utilized to convert the different empirical wavelet components into two-dimensional matrices, and singular values extracted from different matrices were inputted into an SVM can yield gratifying detection results. In [26], arc current was converted to two-dimensional matrix using a Gramian angular summation field, with which the characteristics information of arc current can be enhanced.

The SAF detection methods based on two-dimensional matrix construction have brought beneficial effects to obtaining inspiring detection results. However, the fluctuation patterns of arc currents in PV systems are complex, and the arc-like components caused by power electronic devices pose a great challenge to SAF detection. Therefore, for further enhancing the performance of SAF detection, it is still necessary to investigate the methods of converting one-dimensional arc current into two-dimensional matrix from different perspectives, which is the part of motivation of this article.

Markov transition field (MTF) can mine the state transition information of one-dimensional signals [27]. Compared to the abovementioned matrix transformation methods, MTF provides a unique perspective for analyzing the intrinsic characteristics

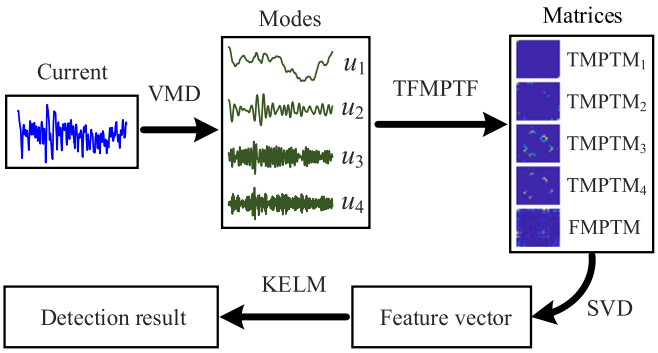

Fig. 1. Flowchart of the proposed method.

of signals [18]. However, MTF lacks the capability to comprehensively analyze state transition characteristics in high-dimensional spaces and time-frequency domains.

To overcome the shortcomings of MTF, the time-frequency Markov permutation transition field (TFMPTF) is proposed in this article. TFMPTF can transform one-dimensional arc current signals into two-dimensional matrixes and extract essential state transition information within arc current from new perspectives. Moreover, this article proposes an SAF detection method by integrating VMD, TFMPTF, and kernel extreme learning machine (KELM), which can promise excellent SAF detection performance for PV systems.

The contributions of this article can be categorized into the following three aspects.

1) A sophisticated mechanism for analyzing the characteristics of state transitions in the time-frequency domain is introduced in TFMPTF. TFMPTF effectively addresses the limitation of MTF, which only examines state transition characteristics from the time domain while overlooking critical dynamic fault information concealed within the frequency domain.
2) An innovative concept of permutation pattern state transitions is introduced in TFMPTF. TFMPTF enables simultaneous analysis of the characteristics of permutation pattern state transitions in both the time and frequency domains. When calculating the transition probabilities of permutation pattern states using TFMPTF, it fully considers the correlations among multiple consecutive data points, thereby overcoming the limitation inherent in MTF, which only addresses the state transition characteristics of individual data points.
3) A SAF detection framework based on VMD, TFMPTF, and KELM is proposed, as illustrated in Fig. 1. Initially, VMD is employed to decompose the current into modes with distinct frequency components. Subsequently, these modes are transformed into two-dimensional matrices using TFMPTF, thereby facilitating the effective acquisition of advanced time-frequency permutation pattern state transition information related to the arc current. Following this step, singular values extracted from the matrices are utilized to construct feature vectors. Finally, KELM is applied to derive detection results.

This article establishes an experimental platform for arc fault detection in PV systems. The platform can simulate the normal operating state and SAF state of the PV system under the three load types (inverter, dc–dc, and resistor). Offline and online experiments are conducted based on this platform. The advanced and robust nature of the proposed SAF detection method is verified by offline comparative experiments. The online experiments indicate that the detection speed of the proposed SAF detection method can meet the requirements of the UL1699B standard [28], and prove that it is suitable for application in PV systems.

II. Variational Mode Decomposition

VMD is a kind of nonrecursive and adaptive signal decomposition method. By iteratively searching for the optimal center frequency and the effective bandwidth of variational problems, signal decomposition can be achieved using VMD. Compared with WT, EMD, and empirical WT, VMD has more advantages in weakening mode confusion, resisting noise interference, and improving decomposition accuracy. SAF can introduce abundant high-frequency noise into the current signal. This article utilizes VMD to decompose the current into different modes, with which the mutual interference between the fault information of different frequency bands can be weakened and the fault features can be extracted more easily.

The pivotal principle of VMD is solving constrained variational problems, which can be expressed as follows:

$$\min_{\{u_k\},\{\omega_k\}} \sum_{k=1}^{K} \left\| \partial_t \left[\left(\delta(t) + \frac{j}{\pi t} \right) * u_k(t) \right] e^{-j\omega_k t} \right\|_2^2 \quad \text{s.t.} \sum_k u_k(t) = S(t) \tag{1}$$

where K represents the number of modes, and $S(t)$ is the arc current to be decomposed. $\delta(t)$ and $*$ represent the Dirac delta function and convolution operation, respectively. $\{u_k\}$ and $\{\omega_k\}$ denote the set of modes and corresponding center frequencies, respectively. $\partial_t\{\cdot\}$ is partial derivative operation over time t. By introducing the penalty coefficient β and the Lagrange multiplier $\lambda(t)$, the constrained optimization problem in (1) can be transformed into an unconstrained optimization problem

$$\begin{aligned} &\mathcal{L}(\{u_k\},\{\omega_k\},) \\ &= \beta \sum_{k=1}^{K} \left\| \partial_t \left[\left(\delta(t) + \frac{j}{\pi t} \right) * u_k(t) \right] e^{-j\omega_k t} \right\|_2^2 \\ &\quad + \left\| x_t - \sum_{k=1}^{K} u_k(t) \right\|_2^2 + \left\langle \lambda(t), x_t - \sum_{k=1}^{K} u_k(t) \right\rangle. \end{aligned} \tag{2}$$

Based on iterative optimization, the values of $\{u_k\}$, $\{\omega_k\}$, and λ can be continuously updated

$$\begin{cases} \hat{u}_k^{n+1}(\omega) = \dfrac{\hat{S}(\omega) - \sum_{i \neq k} \hat{u}_i(\omega) + \frac{\hat{\lambda}(\omega)}{2}}{1 + 2\xi(\omega - \omega_k)^2} \\ \hat{\lambda}^{n+1}(\omega) = \hat{\lambda}^{(n)}(\omega) + \xi\left(\hat{f}(\omega) - \sum_{k=1}^{K} \hat{u}_k^{n+1}(\omega) \right) \\ \omega_k^{n+1} = \dfrac{\int_0^\infty \omega \left| \hat{u}_k^{(n+1)}(\omega) \right|^2 d\omega}{\int_0^\infty \left| \hat{u}_k^{(n+1)}(\omega) \right|^2 d\omega} \end{cases} \tag{3}$$

where $\hat{u}_k^{n+1}(\omega)$, $\hat{S}(\omega)$, and $\hat{\lambda}^{n+1}(\omega)$ are the form of $u_k^{n+1}(t)$, $S(t)$, and $\lambda_k^{n+1}(t)$ after Fourier transform operation. The stopping criteria for the abovementioned iterative operation is $\sum_{k=1}^{K} \frac{\|\hat{u}_k^{n+1}(\omega)-\hat{u}_k^n(\omega)\|_2^2}{\|\hat{u}_k^n(\omega)\|_2^2} < \varepsilon$, ε represents the convergence accuracy.

K is a critical parameter in VMD. If the value of *K* is too small, VMD is not able to effectively separate the arc features from the current signal. If the value of *K* is too large, the computation time will increase seriously. Moreover, a large value of *K* will cause over-decomposition of the signal, leading to duplicate fault information in different modes.

III. Time-Frequency Markov Permutation Transition Field

Converting one-dimensional modes obtained based on VMD into two-dimensional matrices can effectively mine structural information in arc current, which is beneficial for enhancing the performance of SAF detection. This section introduces the basic principles of traditional MTF and proposes TFMPTF to overcome the shortcomings of MTF.

A. Traditional MTF

MTF can analyze the state transition characteristics between adjacent data points [18], [29], which is an effective matrix transformation method. After the decomposition of arc current based on VMD, the mode u_k can be obtained. $u_k = \{u_{k,1}, u_{k,2}, \ldots, u_{k,I}\}$, $k \in \{1, 2, 3, 4\}$, *I* represent the number of data point of u_k. Dividing the value range of the data points of u_k into *q* regions on average, and the MTF with the dimension of $q \times q$ can be calculated using the following equation [27] equation (4) shown at the bottom of this page:

For example, $P(u_{k,i} \in Q_1 | u_{k,i-1} \in Q_2) = \frac{Num_{1,2}}{Num_1}$. $Num_{1,2}$ represents the number of cases that $u_{k,i}$ belongs to the 1-th region Q_1 and $u_{k,i-1}$ belongs to 2-th region Q_2 simultaneously. Num_1 represents the number of cases that $u_{k,i}$ belongs to 1-th region Q_1.

B. Principle of TFMPTF

MTF is capable of capturing the temporal dependencies between adjacent data points; however, there are two shortcomings associated with MTF: 1) MTF only considers the state transition probability between adjacent data points, without adequately considering the correlation between multiple data points in a continuous time period; 2) MTF ignores the data state transition information within the frequency domain.

In this article, TFMPTF is proposed to address the deficiencies in MTF, with which fault features from arc current can be extracted more effectively. First, TFMPTF can calculate the transfer characteristics of permutation pattern states in high-dimensional space from the perspective of the time domain, from which the time Markov permutation transition matrixes (TMPTMs) corresponding to each mode (u_k) can be yielded. Second, TFMPTF is able to analyze the transition probability of permutation pattern states of frequency domain energy (FDE), from which the frequency Markov permutation transition matrix (FMPTM) of arc current $S(t)$ can be obtained.

The method for obtaining TMPTMs and FMPTM of arc current based on TFMPTF is shown as follows.

1) Principle of TMPTMs: The mode u_k of arc current $S(t)$ is converted into high-dimensional matrix UT_k. The *i*th row of matrix UT_k is $UT_{k,i} = \{u_{k,i}, u_{k,i+1}, \ldots, u_{k,i+(m-1)}\}$, $1 \le i \le n-(m-1)$. *m* represents the embedding dimension.

Sorting the data points of $UT_{k,i}$ in ascending order to obtain the corresponding sorted vector $UT_{k,i}^* = \{u_{k,i+(v_1-1)} \le u_{k,i+(v_2-1)} \le \ldots \le u_{k,i+(v_m-1)}\}$. v_1, v_2, …, v_m represent the corresponding indexes of data points in $U_{k,i}$. For example, $v_1 = 2$ represents the value of the second data point ($u_{k,i+1}$) in $U_{k,i}$ is with the smallest value.

Note that a vector $U_{k,i}$ containing *m* data points has a total of *m*! permutation pattern states. Each $UT_{k,i}^*$ corresponds to a unique permutation pattern state πt_g, $g = \{1, 2, \ldots, \mathrm{m}!\}$. According to the concept of MTF, the TMPTM$_k$ corresponding to the mode u_k can be yielded, $k \in \{1, 2, \ldots, K\}$.

For example, $P(UT_{k,i}^* \in \pi t_1 | UT_{k,i-1}^* \in \pi t_2) = \frac{Num_{1,2}}{Num}$. $Num_{1,2}$ represents the number of cases that $UT_{k,i}$ is with permutation pattern state πt_1 and $UT_{k,i-1}$ is with permutation pattern state πt_2 simultaneously. Num represents the number of row vectors in matrix UT_k.

2) Principle of FMPTM: The time-frequency matrix *UF* corresponding to the arc current $S(t)$ is defined in the following equation:

$$UF = \begin{bmatrix} u_1 \\ u_2 \\ \vdots \\ u_K \end{bmatrix} = \begin{bmatrix} u_{1,1} & u_{1,2} & \ldots & u_{1,n} \\ u_{2,1} & u_{2,2} & \ldots & u_{2,n} \\ \vdots & \vdots & \ddots & \vdots \\ u_{K,1} & u_{K,2} & \ldots & u_{K,n} \end{bmatrix} = [uf_1\ uf_2\ \ldots\ uf_n] \tag{6}$$

where u_1, u_2, …, u_K are the *K* modes of arc current $S(t)$, which are obtained based on VMD. $uf_i = [u_{1,i}; u_{2,i}; u_{3,i}; \ldots; u_{K,i}]$ is a column vector containing the components of different frequency bands.

Then the data points of uf_i are arranged in ascending order to obtain the corresponding sorted vector $uf_i^* = \{u_{h_1,i} \le u_{h_2,i} \le \ldots \le u_{h_K,i}\}$. h_1, h_2, …, h_K represent the indexes of the corresponding data points in uf_i. For example, $h_1 = 2$ represents the value of the second data point ($u_{2,i}$) in uf_i is with the smallest value. Each uf_i corresponds to the unique

$$MTM = \begin{bmatrix} P(u_{k,i} \in Q_1 | u_{k,i-1} \in Q_1) & \ldots & P(u_{k,i} \in Q_1 | u_{k,i-1} \in Q_q) \\ \vdots & \ddots & \vdots \\ P(u_{k,i} \in Q_q | u_{k,i-1} \in Q_1) & \ldots & P(u_{k,i} \in Q_q | u_{k,i-1} \in Q_q) \end{bmatrix}. \tag{4}$$

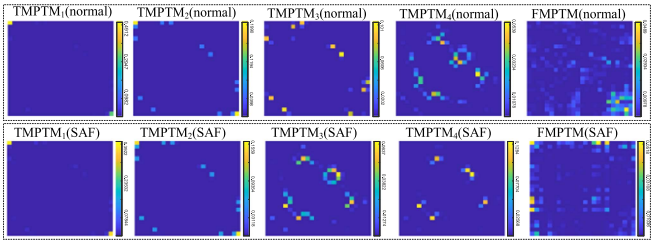

Fig. 2. Images of TMPTMs and FMPTM under normal and SAF conditions.

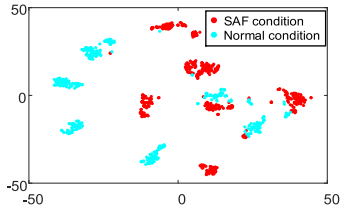

Fig. 3. t-SNE visualization of singular values under SAF and normal conditions.

permutation pattern πf_g, $g = \{1, 2, \ldots, K!\}$. According to the concept of MTF, the FMPTM of current signal $S(t)$ can be obtained.

For example, $P\quad (uf_i^* \in \pi f_1 | uf_{i-1}^* \in \pi f_2) = \frac{Num_{1,2}}{Num}$. $Num_{1,2}$ represents the number of cases that uf_i^* is with permutation pattern πf_1 and uf_{i-1}^* is with permutation pattern πf_2 simultaneously. Num represents the number of column vectors in matrix UF.

3) Parameter Selection and Calculation Results of TFMPTF: According to (5) and (7) shown at the bottom of this page, TMPTMs and FMPTM obtained based on TFMPTF are matrices with the size of $m! \times m!$ and $K! \times K!$. The sizes of TMPTMs and FMPTM are determined by parameter *m* and parameter *K*, respectively, and parameter *K* controls the number of TMPTMs as well. Based on the analysis in the last paragraph of Section II, *K* is set to 4 in this article to obtain the best decomposition performance of VMD. Therefore, the size of FMPTM is 24×24, and the number of TMPTMs is 4.

If the value of parameter *m* is too small, the permutation pattern information in the signal cannot be fully mined. If the value of parameter m is too large, the size of TMPTMs will be too large, and the calculation time of subsequent feature extraction will increase. Moreover, the redundant fault information introduced by a large value of *m* is not conducive to the improvement of detection performance. In this article, *m* is set to 4 to obtain satisfactory detection performance, and the sizes of TMPTMs are 24×24.

Fig. 2 shows the images of TMPTMs and FMPTM under normal and SAF conditions, respectively. The image textures corresponding to normal and SAF conditions are significantly different, from which it is indicated that the time-frequency permutation pattern state transfer information mined based on TFMPTF can effectively distinguish between normal and SAF conditions.

IV. Singular Value Decomposition

The singular values of arc current contain the pivotal fault information, singular value decomposition (SVD) is an effective feature extraction method [24]. In this article, the singular values of two-dimensional matrices (TMPTMs and FMPTM) are extracted by SVD to construct high-dimensional feature vectors.

The singular values of a matrix A with the size of $L \times L$ can be calculated: $A = HSV^T$. $S = [diag(\delta_1, \delta_2, \ldots, \delta_L)] \in R^{L \times L}$ represents a diagonal matrix. $\delta_1, \delta_2, \ldots, \delta_L$ are the singular values of matrix *A*, and $\delta_1 > \delta_2 > \ldots > \delta_L > 0$. $H = [h_1, h_2, \ldots, h_L] \in R^{L \times L}$, $V = [v_1, v_2, \ldots, v_L] \in R^{L \times L}$. *H* and *V* belong to orthogonal matrices.

In this article, TMPTMs and FMPTM are with the size of 24×24 simultaneously. Therefore, for a sample of arc current, $24 \times 5 = 120$ singular values can be extracted, and the dimension of the feature vector constructed based on singular values is 120. Fig. 3 shows the t-SNE visualization of singular values under SAF conditions and normal conditions. The most singular values under SAF conditions and normal conditions have good differentiation, and only a small number of data points appear in state confusion, from which the validity of the extracted features is proved.

This article uses KELM to process the extracted features, with which the complex nonlinear relationship between feature vectors and fault types can be adequately explored.

V. Kernel Extreme Learning Machine

Huang et al. [30] proposed KELM by introducing the kernel function principle into ELM. KELM not only inherits the

$$\text{TMPTM}_k = \begin{bmatrix} P\left(UT_{k,i}^* \in \pi t_1 | UT_{k,i-1}^* \in \pi t_1\right) & \ldots & P\left(UT_{k,i}^* \in \pi t_1 | UT_{k,i-1}^* \in \pi t_{m!}\right) \\ \vdots & \ddots & \vdots \\ P\left(UT_{k,i}^* \in \pi t_{m!} | UT_{k,i-1}^* \in \pi t_1\right) & \ldots & P\left(UT_{k,i}^* \in \pi t_{m!} | UT_{k,i-1}^* \in \pi t_{m!}\right) \end{bmatrix}. \tag{5}$$

$$\text{FMPTM} = \begin{bmatrix} P\left(uf_i^* \in \pi f_1 | uf_{i-1}^* \in \pi f_1\right) & \ldots & P\left(uf_i^* \in \pi f_1 | uf_{i-1}^* \in \pi f_{K!}\right) \\ \vdots & \ddots & \vdots \\ P\left(uf_i^* \in \pi f_{K!} | uf_{i-1}^* \in \pi f_1\right) & \ldots & P\left(uf_i^* \in \pi f_{K!} | uf_{i-1}^* \in \pi f_{K!}\right) \end{bmatrix}. \tag{7}$$

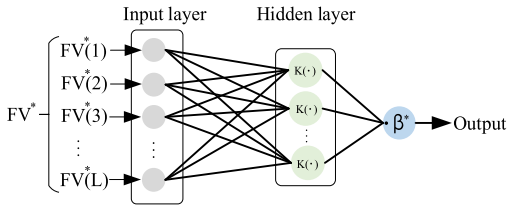

Fig. 4. Structure diagram of KELM.

advantage of ELM's fast training speed but also has more advantages in generalization ability than ELM, SVM, and artificial neural networks [31]. Fig. 4 shows the structure of KELM.

Supposing that the training dataset containing Q feature vectors is $\{\mathrm{FV}^1, \mathrm{FV}^2, \ldots, \mathrm{FV}^Q\}$, and the sample to be tested is FV^*. The output result of KELM with kernel function $K(\cdot)$ is shown as follows:

$$f(\mathrm{FV}^*) = \begin{bmatrix} K(\mathrm{FV}^*, \mathrm{FV}^1) \\ \vdots \\ K(\mathrm{FV}^*, \mathrm{FV}^Q) \end{bmatrix}^T \left(HH^T + \tau I\right)^{-1} T \tag{8}$$

$$HH^T = \begin{bmatrix} K(\mathrm{FV}^1, \mathrm{FV}^1) & \ldots & K(\mathrm{FV}^1, \mathrm{FV}^Q) \\ \vdots & \ddots & \vdots \\ K(\mathrm{FV}^Q, \mathrm{FV}^1) & \ldots & K(\mathrm{FV}^Q, \mathrm{FV}^Q) \end{bmatrix} \tag{9}$$

where τ denotes the regularization parameter and is significantly related to the stability of the KELM's output.

As shown in Fig. 4, $\beta^* = \left(HH^T + \tau I\right)^{-1} T$ is output matrix. This article utilizes the radial basis function as the kernel function. $K(\cdot) = \exp(-\frac{\|\mathrm{FV}^* - \mathrm{FV}^q\|}{2\delta^2})$, and parameter δ can control the perceived range of $K(\cdot)$. In this article, particle swarm optimization (PSO) is applied to search the two key parameters τ and δ of KELM [32], [33].

VI. Experimental Platform and Data Collection

The experimental platform (in Fig. 5) is established in this article to verify the performance of the proposed method. PV simulated source can simulate the volt-ampere characteristics of solar cells and can provide direct current energy to the load. The three types of commercial loads are the inverter, dc–dc, and resistor. The selector switch can control the selection of load type. The electric arc generator is connected in series to the circuit. When the system is powered on, SAF can be caused by separating the two electrodes of the arc generator to a certain distance based on the arc length controller.

This platform uses a current sensor to collect arc current. The analog signal outputted by the current sensor is converted into a digital signal by the data acquisition (DAQ) board and then the digital signal is transmitted to the microprogrammed control unit (MCU). Since arc characteristics are mainly reflected in the frequency band less than 100 kHz [26], [34], the sampling rate of the DAQ board is set to 200 kHz in this article. The MCU can analyze the collected data online or save the collected data. PC can download the saved data in MCU via USB.

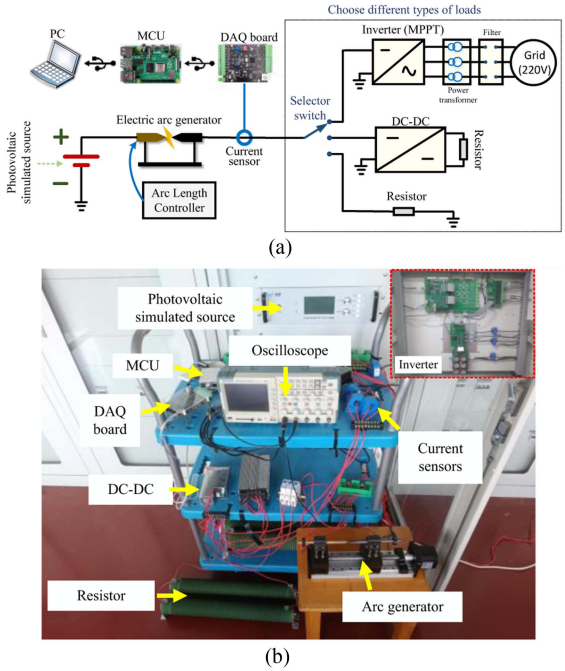

Fig. 5. Experimental platform. (a) Diagram. (b) Actual platform.

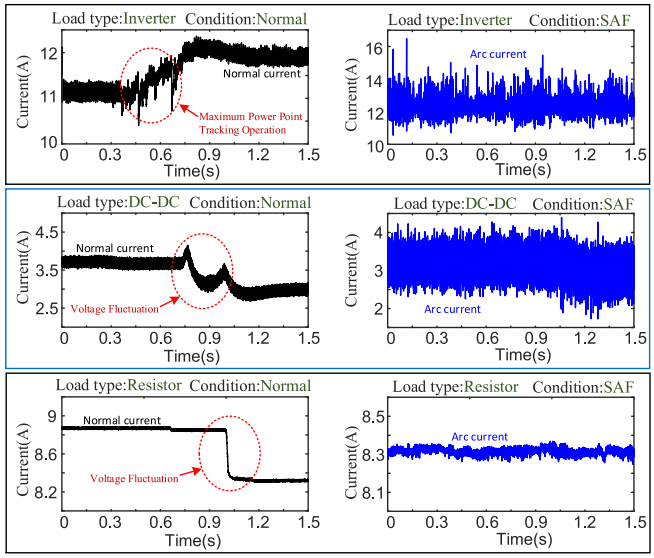

Fig. 6. Normal current and arc current under different types of loads.

Python 3.7 is used in both MCU and PC to implement algorithm programming. The MCU is equipped with an ARM Cortex-A72 CPU. The PC has a Windows 11 operating system, intel i5-12500H CPU, and NVIDIA RTX 3050 GPU, respectively, and the size of RAM of the PC is 32 GB.

Fig. 6 presents the normal current and arc current under different types of loads. Under SAF conditions, the randomness of the current signal is enhanced, and the amplitude of fluctuation is increased. Since inverter and dc–dc are nonlinear loads, the current fluctuation degree under inverter and dc–dc is greater than that under resistor (linear load). Under normal conditions,

TABLE I
EXPERIMENTAL CONDITIONS CORRESPONDING TO THE DATASET

State	Voltage (V)	Current (A)	Label	Number of samples	Load type
Normal condition	250~400	6~17	1	5800	Inverter
	80~150	2~8		2500	DC-DC
	50~400	2~17		2500	Resistor
SAF condition	250~400	6~17	2	5800	Inverter
	80~150	2~8		2200	DC-DC
	50~400	2~17		2200	Resistor

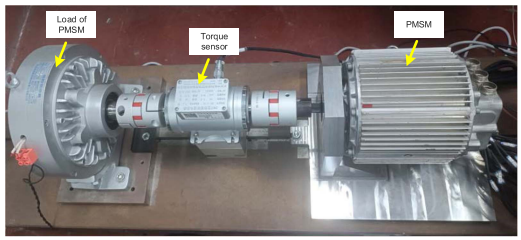

Fig. 7. Experimental platform of PMSM traction system.

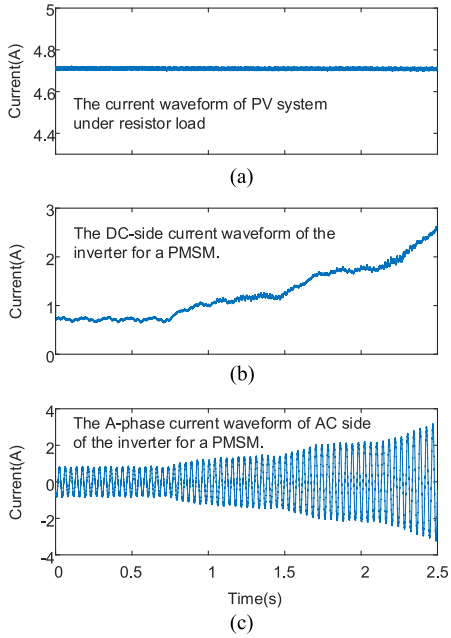

Fig. 8. Current waveform diagrams of different circuits during the PMSM load change process. (a) Current waveform of PV system under resistor load. (b) DC-side current waveform of the inverter for a PMSM. (c) A-phase current waveform of ac side of the inverter for a PMSM.

the current signal has good stationarity. However, transient actions such as MPPT operation and voltage fluctuation will introduce arc-like components into the current signal.

In this article, 31 500 samples are collected based on the established experimental platform, among which 18 900 samples are used to construct a training set, and the remaining 12 600 samples were used as a test set. Each sample contains 1024 data points. The experimental conditions corresponding to the dataset are shown in Table I. When the load type is an inverter, a total of 11 600 samples are collected, comprising 5800 samples under normal conditions and 5800 samples under SAF conditions. The operational voltage range of the inverter is between 250 and 400 V, while the current range spans from 6 to 17 A. In the case of a dc–dc converter, as the load type, a total of 4700 samples are gathered, this includes 2500 samples under normal conditions and 2200 samples under SAF conditions. The voltage range during operation for the dc–dc converter is between 80 and 150 V, with a current range from 2 to 8 A. Lastly, when using a resistor as the load type, another set of 4700 samples is collected—comprising again of 2500 samples under normal conditions and another set of 2200 samples under SAF conditions. The operational voltage range in this scenario extends from 50 to 400 V and the current ranges from 2 to 17 A. Note that normal samples contain transient conditions (output voltage fluctuation of PV source and starting process of loads).

This article also studies the influence of adjacent permanent magnet synchronous motor (PMSM) traction systems on the obtained current signals. The experimental platform of the PMSM traction system is shown in Fig. 7. This platform is adjacent to the PV system, with a distance of 3 m. The PMSM used in the system is sourced from an electric vehicle, with a maximum power of 10 kW. Fig. 8 shows the current signals collected from the PV system and the PMSM traction system during the load perturbation of the PMSM. The rotational speed of the PMSM is 400 r/min. As shown in Fig. 8(b) and (c), when the load of the PMSM exists a nonlinear sudden increase, the dc side and ac side current signals of the PMSM inverter increase correspondingly. In this complex electromagnetic environment, the current signal collected using the current sensor is not contaminated with additional noise, as shown in Fig. 8(a). Therefore, the current signal collected from the PV system using a current sensor will not be affected by the complex electromagnetic working state of the adjacent system.

TABLE II
DETECTION RESULTS OF PROPOSED METHOD UNDER DIFFERENT EXPERIMENTAL CONDITIONS

State	Load type	Detection results
Normal condition	Inverter	99.11% (3449/3480)
	DC-DC	98.86% (1483/1500)
	Resistor	99.93% (1499/1500)
SAF condition	Inverter	98.62% (3432/3480)
	DC-DC	98.56% (1301/1320)
	Resistor	99.01% (1307/1320)
The overall detection accuracy is 98.97% (12471/12600)		

VII. EXPERIMENTAL RESULTS ANALYSIS

A. Detection Results of Proposed Method in Offline Environment

This article verifies the performance of the proposed method based on the collected data in an offline environment. The detection results of the proposed method under different experimental conditions are given in Table II. The overall detection accuracy is 98.97% (12 471/12 600). The detection accuracy under normal and SAF conditions is 99.24% (6431/6480) and 98.69% (6040/6120), respectively. The proposed method can not only accurately implement SAF detection, but also can effectively

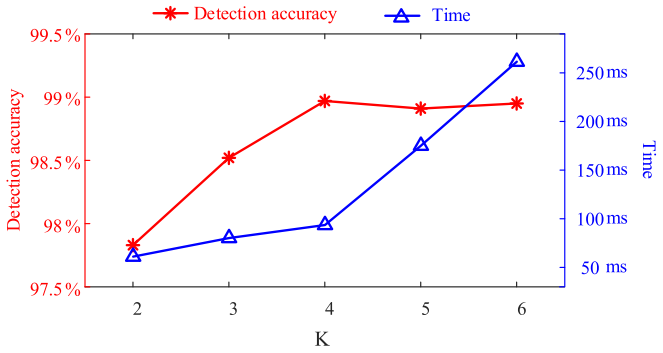

Fig. 9. Detection accuracy and the feature extraction time with different values of K.

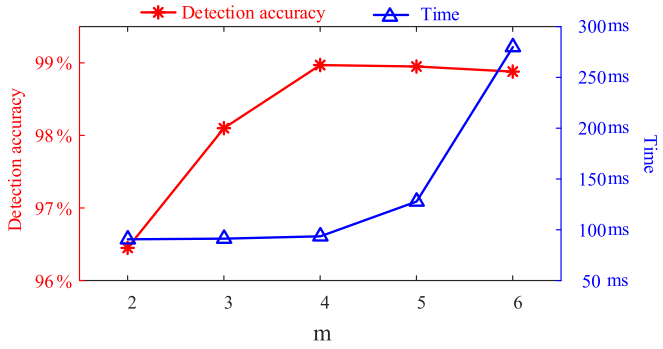

Fig. 10. Detection accuracy and the feature extraction time with different values of m.

suppress false alarms under normal conditions. Since SAF can lead to a complex random fluctuation of the current signal, the detection accuracy under normal conditions is higher than that under SAF conditions, from which the difficulty of detection is increased.

Under normal conditions, the detection accuracy corresponding to the resistor load (99.93%) is higher than that corresponding to the inverter (99.11%) and dc–dc (98.86%). This is because the resistor is a linear load, whereas the inverter and dc–dc converter are nonlinear loads. The high-frequency switching operation of nonlinear loads will introduce complex noise in the current signal, and the transient operation time of nonlinear load is longer than that of linear load. Consequently, under normal conditions, inverters and dc–dc converters are more likely to generate false alarms for detection algorithms compared to resistors.

Under SAF conditions, the detection accuracy associated with resistors (99.01%) is higher than that of inverters (98.62%) and dc–dc converters (98.56%). Both inverters and dc–dc incorporate internal power control mechanisms. When arc faults occur within the system with inverters and dc–dc, the unstable fluctuations introduced by these faults can disrupt the stable operating range of their control algorithms, resulting in stronger and more complex oscillation patterns within the current signal. Therefore, relative to resistors, both inverters and dc–dc converters complicate SAF detection.

The number of modes K and the embedding dimension m are the key parameters in the proposed TFMPTF.

Fig. 9 illustrates the detection accuracy and feature extraction time across different values of K. When K is small, VMD decomposes the arc current into a limited number of modes, resulting in a shorter computation time for the VMD decomposition process. With fewer modes, there are also fewer TFMPTMs to process, consequently, the feature extraction time tends to decrease as K decreases. However, if K is too small, it may not adequately separate the fault features within the arc current, which hinders accurate SAF detection. Conversely, if K is excessively large, it can lead to over-decomposition of the arc current. While this significantly increases computation time, further improvements in detection accuracy become challenging. As K increases, detection accuracy initially rises. However, once K exceeds 4, detection accuracy stabilizes while feature extraction time markedly increases. Therefore, this article sets K at 4.

Fig. 10 illustrates the detection accuracy and feature extraction time across varying values of m. When the value of m is too small, the vector encompasses insufficient states to effectively capture abrupt changes in arc current dynamics. Conversely, if m is excessively large, it significantly enlarges the size of the TFMPTMs, thereby prolonging the time required for singular value extraction. Additionally, a high value of m may lead to homogenization among different vectors, resulting in excessive redundant information. As depicted in Fig. 10, when m is less than 4, detection accuracy falls below 98.1%. Upon exceeding this threshold, detection accuracy experiences a slight decline but remains above 98.8%. For values of m less than or equal to 4, feature extraction time stabilizes around 93 ms. However, once m surpasses 4, feature extraction time escalates rapidly in an exponential manner with increasing values of m. Therefore, taking into account both detection accuracy and feature extraction time considerations, this study establishes m at a value of 4.

In this article, KELM is employed as the classifier to achieve precise detection results. The selection of parameters τ and δ significantly influences KELM's performance. To ensure optimal classification efficacy, a five-fold cross-validation method is implemented during the training process to assess KELM's performance across various parameter combinations. This method partitions the training set into five equal-sized subsets, utilizing four for training KELM while reserving one for validation purposes. This procedure is repeated five times, with each iteration selecting a different subset as the test set and using the remaining subsets for validation. Ultimately, the average of these five evaluation results yields the final validation accuracy.

Fig. 11 illustrates the validation accuracy corresponding to different values of τ and δ. As τ and δ fluctuate, the validation accuracy displays multiple peaks along with pronounced nonlinearity; furthermore, there exists a strong coupling between τ and δ. The traditional grid search method for determining the key parameters of KELM suffers from issues related to insufficient precision and low search efficiency. PSO is a heuristic optimization algorithm that does not rely on gradient information, making it well-suited for tackling optimization problems characterized by multiple peaks, discontinuities, and nonlinearity. In this study,

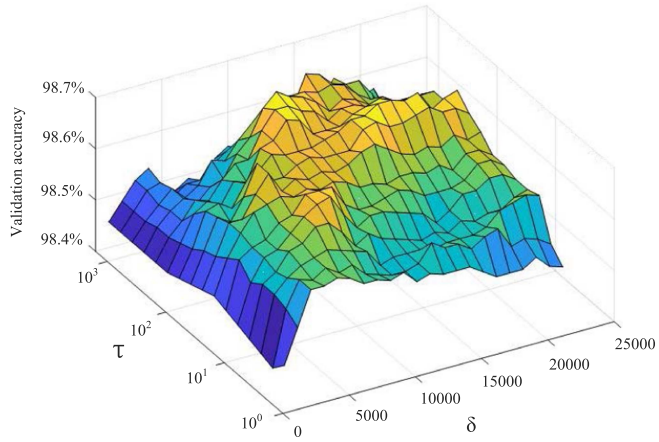

Fig. 11. Validation accuracy under different values of τ and δ.

PSO is employed to identify the two critical parameters τ and δ of KELM [32]. Prior to utilizing PSO for parameter extraction in KELM, it is essential to establish the search ranges for the parameters under optimization, configure the internal settings of PSO, and construct an appropriate objective function. The designated search ranges for τ and δ are set as [0, 1000] and [0, 22 000], respectively. The internal parameters of PSO include the inertia factor ω as well as learning factors C_1 and C_2. Based on [33], ω, C_1 and C_2 are configured at 1.45, 0.729, and 0.729, respectively. The cross-validation accuracy obtained during KELM training serves as the fitness value in the parameter optimization process.

The core principle of optimizing the key parameters of KELM using PSO involves the continuous evaluation of fitness values for various parameter combinations throughout the iterations, with higher fitness values indicating superior combinations. In this study, the PSO population is configured to consist of 30 individuals, and a total of 500 iterations are performed. The final optimization results yield $\tau = 398.1$ and $\delta = 11684.2$.

B. Performances Comparison of Different Feature Extraction Methods in an Offline Environment

In this article, the performance of the proposed feature extraction method (PF) is compared with nine different feature extraction methods. The features obtained based on different feature extraction methods are input into KELM to yield detection results. It is important to note that, in order to compare the stability and robustness of various feature extraction methods, each method is executed 30 times. In each experiment, 18 900 samples are randomly selected to construct the training set, while 12 600 samples are used for the test set. Subsequently, the average detection accuracy and standard deviation (Std) of detection accuracy for different feature extraction methods are calculated.

Feature extraction method CF_1: CF_1 uses traditional MTF and SVD to extract features. First, the MTF of the current signal is constructed, and then the singular values of the MTF are extracted to construct the feature vector. CF_1 can be used to verify whether the performance of the proposed TFMPTF is superior to that of traditional MTF.

Feature extraction method CF_2 [23]: CF_2 is based on the RQA of RP. First, the RP of arc current is constructed. Then perform RQA on RP to obtain recurrence rate, determinism, entropy, and averaged diagonal line length to construct the feature vector. In [23], embedding dimension, time delay, and criterion threshold are 4, 2, and 0.6021, respectively.

Feature extraction method CF_3 [24]: CF_3 is based on IRP, RQA and SVD. CF_3 extracts RQA-based features (recurrence rate, determinism, entropy, averaged diagonal line length) and five maximum singular values to construct the feature vector. In CF_3, the embedding dimension and time delay are 4 and 2, respectively.

Feature extraction method CF_4 [11]: CF_4 constructs feature vectors by extracting current variance (Var), pulse factor (PUF), kurtosis factor (KF), and wavelet energy entropy (WTEnt). The type of wavelet basis function used in CF_4 is db4.

Feature extraction method CF_5 [12]: CF_5 is based on VMD and multiscale fuzzy entropy (MFE). First, the arc current is decomposed into four components by using VMD, and the fuzzy entropy of first mode and second mode are extracted under the first five scales to construct a 10-dimensional feature vector. The embedded dimension, gradient, and border width of MFE are 3, 2, and 0.15, respectively.

Feature extraction method CF_6 [35]: CF_6 is a feature extraction method based on EMD, FDE, min-to-max value (MMV), and Var. First, arc current is decomposed into modes by the EMD. Then the FDE, MMV, and Var are extracted from modes to construct four-dimensional fault feature vector.

Feature extraction methods CF_7, CF_8, and CF_9: The primary distinction between PF and the three comparative methods (CF_7, CF_8, and CF_9) resides in their respective dimension reduction techniques. CF_7 is a principal component analysis (PCA) [36] based method. CF_8 is a linear discriminant analysis (LDA) [37] based method. CF_9 is a non-negative matrix factorization (NNMF) [38] based method. PCA, LDA, and NNMF are three representative dimensionality reduction techniques. Each matrix (TMPTMs and FMPTM) is compressed into a 24-dimensional vector through PCA, LDA, or NNMF. Consequently, the dimension of the fault feature vectors in CF_7, CF_8, and CF_9 matches that of PF.

Table III presents the performance of the proposed feature extraction method (PF) and nine comparative feature extraction methods (CF_1, CF_2, CF_3, CF_4, CF_5, CF_6, CF_7, CF_8, and CF_9). The average detection accuracy of PF, CF_1, CF_2, CF_3, CF_4, CF_5, CF_6, CF_7, CF_8, and CF_9 are 98.97%, 93.02%, 94.03%, 97.75%, 92.06%, 97.38%, 95.17%, 98.30%, 91.81%, and 97.05%, respectively. The Std of accuracy of PF, CF_1, CF_2, CF_3, CF_4, CF_5, CF_6, CF_7, CF_8, and CF_9 are 0.08%, 0.24%, 0.20%, 0.18%, 0.25%, 0.20%, 0.22%, 0.13%, 0.23%, and 0.16%, respectively.

The average detection accuracy of PF is 5.95% higher than that of CF_1, indicating that the performance of the feature extraction method based on VMD and TFMPTF is superior to that based on traditional MTF. Compared with MTF, the proposed method can mine the state transition information hidden

TABLE III
OFFLINE PERFORMANCE OF DIFFERENT FEATURE EXTRACTION METHODS

	Method	Feature extraction time	Average detection accuracy	Std of accuracy
PF	VMD+TFMPTF+ SVD	93.8ms	98.97%	0.08%
CF_1	MTF+SVD	4.86ms	93.02%	0.24%
CF_2	RP+RQA [23]	36.1ms	94.03%	0.20%
CF_3	IRP+RQA+ SVD [24]	47.2ms	97.75%	0.18%
CF_4	Var+PUF+KF+ WTEnt [11]	1.54ms	92.06%	0.25%
CF_5	VMD+MFE [12]	759.1ms	97.38%	0.20%
CF_6	EMD+Var+MMV + FDE [35]	5.9ms	95.17%	0.22%
CF_7	VMD+TFMPTF+ PCA [36]	93.2ms	98.30%	0.13%
CF_8	VMD+TFMPTF+ LDA [37]	92.7ms	91.81%	0.23%
CF_9	VMD+TFMPTF+ NNMF [38]	101.43ms	97.05%	0.16%

in the time-frequency domain more effectively. The detection accuracy of PF is significantly higher than that of the other nine state-of-the-art feature extraction methods, which further proves the advancement and effectiveness of the proposed feature extraction method. Although the feature extraction time of CF_1, CF_4, and CF_6 is below 10 ms; however, the average detection accuracy of CF_1, CF_4, and CF_6 are not satisfactory (below 96%). A comparison of the experimental results for PF, CF_7, CF_8, and CF_9 indicates that the detection accuracy achieved using PCA, LDA, and NNMF is inferior to that obtained through SVD. The feature extraction times for PCA and LDA are comparable to those of SVD. However, the feature extraction time for NNMF is greater than that of SVD. Consequently, the overall performance of SVD surpasses that of PCA, LDA, and NNMF. The Std of accuracy for PF is 0.08%, which is lower than those associated with other feature extraction methods.

The feature extraction time of CF_2 and CF_3 are around 40 ms, which does not differ by an order of magnitude from that of the proposed method (93.8 ms). The feature extraction time of CF_5 (759.1 ms) is the largest among the feature extraction seven methods. In terms of feature extraction time, the proposed method does not have absolute advantages, however, which is still acceptable. Standard UL1699B stipulates that the arc fault detection time should not be more than 2.5 s [28], [39], and Section VII-D will verify whether the online detection speed of the proposed method could satisfy the requirements of the standard.

Under varying training and testing datasets, the proposed feature extraction method achieves a higher average detection accuracy and a lower Std of accuracy compared to nine reference methods. The method presented in this article demonstrates enhanced effectiveness in mitigating the interference of unknown states within test samples on detection results when compared to these nine methods. The robustness, stability, and scalability of the proposed feature extraction method have been validated.

TABLE IV
OFFLINE PERFORMANCE OF DIFFERENT CLASSIFICATION METHODS

Method	Training time	Average detection accuracy	Std of accuracy
KELM	4.44 s	98.97%	0.08%
RF	1.95 s	98.37%	0.12%
ABT	4.86 s	95.49%	0.28%
GRBT	12.14 s	95.63%	0.31%
HiGRBT [40]	3.85 s	98.56%	0.11%
ET	0.39 s	98.22%	0.12%
SVM	2.07 s	98.50%	0.10%
NN	43.61 s	98.09%	0.13%
EHCNN [41]	816 s	98.98%	0.05%
LOCALVIT [42]	2843 s	97.25%	0.16%
RESNET18 [43]	3892 s	98.71%	0.10%
VGG16 [44]	8685 s	98.02%	0.09%

C. Performances Comparison of Different Classification Methods in Offline Environment

In this article, the KELM used in the proposed method is compared with 10 classification methods. RF, AdaBoost (ABT), GradientBoosting (GRBT), HistGradientBoosting (HiGRBT) [40], and extra trees (ET) are ensemble methods. SVM and neural network (NN) are traditional machine learning algorithms. The features used for KELM, RF, AdaBoost, GradientBoosting, HistGradientBoosting, SVM, and NN are extracted based on the proposed feature extraction method. Enhanced convolutional neural network (EHCNN) [41], Locality to Vision Transformers (LOCALVIT) [42], RESNET18 [43], and VGG16 [44] are deep learning methods, note that those deep learning methods use the original current signal as the input.

In RF, ABT, GRBT, and ET, the tree number is 50. In HiGRBT, the maximum number of iterations is 200. In SVM, the parameters of penalty σ and kernel function ρ are selected using PSO. In NN, the maximum number of training times is 200, the learning rate is 0.001 and the network structure is [120, 50, 1]. The learning rates of EHCNN, LOCALVIT, RESNET18, and VGG16 are 6×10^{-4}, 1×10^{-5}, 2×10^{-6}, and 1×10^{-4}. For more details on EHCNN, LOCALVIT, RESNET18, and VGG16, please refer to [41], [42], [43], and [44], respectively. In order to obtain optimal performance, the parameters in the abovementioned models are selected carefully.

In this section, the performance of various classification methods is compared based on statistical results from 30 runs. In each experiment, 18 900 samples and 12 600 samples are randomly selected to form the training set and test set, respectively.

Table IV demonstrates that the average detection accuracy of KELM (98.97%) is superior to that of RF (98.37%), ABT (95.49%), GRBT (95.63%), HiGRBT (98.56%), ET (98.22%), SVM (98.50%), and NN (98.09%). The Std of the accuracy of KELM (0.08%) is lower than those of RF (0.12%), ET (0.12%), ABT (0.28%), GRBT (0.31%), HiGRBT (0.11%), SVM (0.10%), and NN (0.13%). This indicates that KELM exhibits more stable detection results compared to these seven machine-learning methods. The training time of KELM is inferior to that of RF (1.95 s), ET (0.39 s), HiGRBT (3.85 s), and SVM (2.07 s), and is superior to that of ABT (4.86 s), GRBT (12.14 s), and NN (43.61 s). Considering the detection accuracy

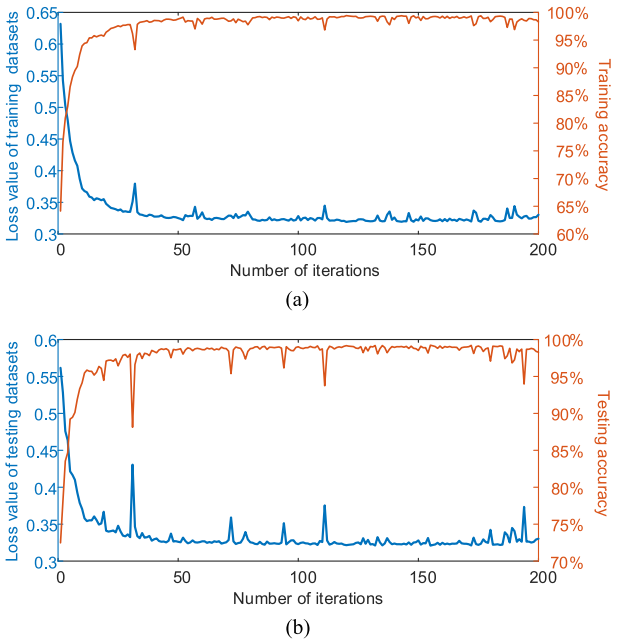

Fig. 12. Loss curve and accuracy curve of EHCNN. (a) Relating to training datasets. (b) Relating to testing datasets.

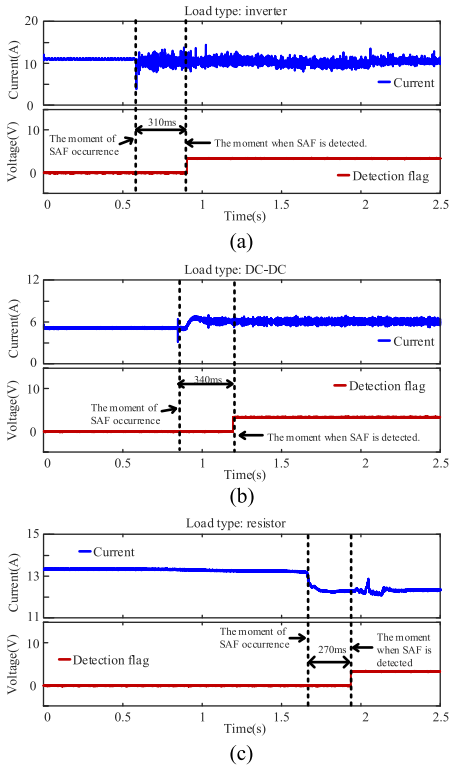

Fig. 13. Online detection results under SAF conditions. (a) Inverter load. (b) DC–DC. (c) Resistance load.

and training time comprehensively, KELM is of advantages over the five ensemble methods (RF, ET, ABT, GRBT, and HiGRBT) and two traditional machine learning methods (SVM and NN).

Four deep learning methods can mine fault characteristics in arc current based on deep network structure, but only EHCNN (98.98%) has a slightly higher average detection accuracy than KELM (98.97%). The average detection accuracy of LOCALVIT (97.25%), RESNET18 (98.71%), and VGG16 (98.02%) is lower than that of KELM. The training time of KELM is much smaller than those of EHCNN (816 s), LOCALVIT (2843 s), RESNET18 (3892 s), and VGG16 (8685 s). Fig. 12 depicts the loss curve and accuracy curve of EHCNN. Fig. 12(a) pertains to the training datasets, and Fig. 12(b) relates to the testing datasets. As the iterative training proceeds, the loss value of both the testing and training datasets initially decreases rapidly, and the training accuracy and testing accuracy increase promptly. This is because the model's performance is suboptimal at the outset, and the initial training can enhance the model's performance swiftly. As the iterative training continues, the model's performance gradually improves. The rate of decrease in the loss value of the testing and training datasets slows down, and the rate of increase in the training accuracy and testing accuracy also diminishes. When the number of iterations reaches 150, the variations in the loss curve and accuracy curve become stable. During the training process of EHCNN, there are fluctuations in the loss curve and accuracy curve, because the model parameters are updated based on the gradient descent method, this makes the improvement of the model's performance somewhat random and cannot guarantee that the model's performance is superior to that of the previous iteration in each training. EHCNN, LOCALVIT, RESNET18, and VGG16 have complex network structures, and the training process of deep learning methods is very time-consuming. Moreover, the training of these four deep learning methods requires additional GPU acceleration, and the hardware cost of training these four deep learning models is also much higher than KELM. The Std of the accuracy of KELM (0.08%) is only higher than EHCNN but lower than the other nine methods. The experimental results derived from various training sets and testing sets demonstrate that the robustness, stability, and scalability of KELM are competitive among the 11 classification methods. Therefore, among the twelve classification methods, the detection performance of KELM is very competitive.

D. Online Experimental Results Analysis

The proposed method is implemented in MCU for online SAF detection to further verify the detection speed. This study also presents the waveforms of the detection flag under various scenarios.

The detection accuracy under inverter, dc–dc, and resistor is 96.66% (58/60), 98.33% (59/60), and 100% (60/60), respectively. Fig. 13 shows the online detection results under the different load types. For example, in Fig. 13(a), after 310 ms of SAF occurrence, the detection flag output by MCU could change by a step, indicating that SAF occurred in this system. The maximum detection time during online experiments is less than 400 ms, which satisfies the requirement of UL1699B that the detection time should be less than 2.5 s [28], [39].

This article also verifies whether the proposed method can effectively avoid false alarms under unknown transient

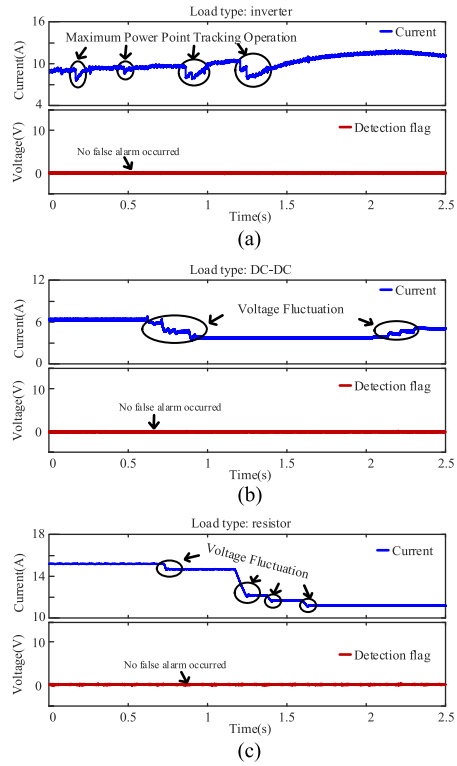

Fig. 14. Online detection results under transient conditions. (a) Inverter load. (b) DC–DC. (c) Resistance load.

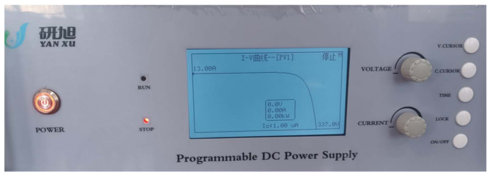

Fig. 15. Operation interface of the PV simulated source.

conditions, as shown in Fig. 14. Unknown transient conditions include MPPT operation of the inverter, voltage fluctuation of dc–dc, and voltage fluctuation of resistance load. The amplitude and direction of the fluctuations are unknown for the proposed SAF detection method. It should be noted that the PV-simulated source employed in this article is capable of simulating the V-I characteristics of actual PV cells. The operation interface of the PV simulated source is depicted in Fig. 15. The PV simulated source is produced by Yanxu Electric. The model of this PV simulated source is YXMG-PVG05, with a capacity of 5 kW and a maximum output voltage of 500 V. At a low voltage range, the PV cell is approximately a constant current source. Once the voltage exceeds a certain value, the V-I characteristics of the PV cell turn nonlinear, that is, the current drops rapidly as the voltage rises. The inverter can regulate the output voltage of the PV cell to enable it to output the maximum power, a process known as MPPT. By rotating the adjustment knob, the open-circuit voltage and short-circuit current shown in Fig. 15 can be modified conveniently to simulate the effect of actual

TABLE V
ONLINE DETECTION RESULTS OF DIFFERENT FEATURE EXTRACTION METHODS

	Method	Online detection time	Online detection accuracy
PF	VMD+TFMPTF+ SVD	332.89 ms	99%
CF_1	MTF+SVD	85.14 ms	94.00%
CF_2	RP+RQA [23]	157.28 ms	94.67%
CF_3	IRP+RQA+ SVD [24]	211.46 ms	98.33%
CF_4	Var+PF+KF+ WTEnt [11]	69.40 ms	91.00%
CF_5	VMD+MFE [12]	3059.35 ms	98.33%
CF_6	EMD+Var+MMV+ FDE [35]	113.51 ms	96.67%
CF_7	VMD+TFMPTF+ PCA [36]	356.46 ms	98.66%
CF_8	VMD+TFMPTF+ LDA [37]	341.18 ms	93.33%
CF_9	VMD+TFMPTF+ NNMF [38]	327.25 ms	98%

TABLE VI
ONLINE DETECTION RESULTS OF DIFFERENT CLASSIFICATION METHODS

Method	Online detection time	Online detection accuracy
KELM	332.89 ms	99%
RF	307.51 ms	98%
ABT	264.82 ms	94.67%
GRBT	269.73 ms	96.33%
HiGRBT [40]	288.16 ms	98.66%
ET	372.44 ms	98.33%
SVM	396.28 ms	99%

light intensity changes on the V-I characteristics of a PV cell. As a result, the maximum power point of the PV cell will also change along with the variation in the V-I characteristics, and the inverter will trace a new maximum power point, leading to fluctuations in the line current. In Fig. 14(a), the area encircled by the dashed line represents the simulation of the changes in the V-I characteristics of the PV cell due to changes in light intensity, which is characterized by a significant fluctuation in the current signal, but the detection flag does not change at the corresponding moment. Therefore, changes in light intensity cannot trigger a false alarm. Under the different load types, 40 unknown transient conditions are generated, respectively, and no misjudgment occurs, from which the robustness and scalability of the proposed detection method are verified.

The comparison feature extraction methods in Table III are implemented using Python programming language, which can be readily migrated to the MCU for online SAF detection. In Table IV, some of the classification methods (NN, EHCNN, LOCALVIT, RESNET18, and VGG16) are programmed based on PyTorch during offline experiment, however, there is a compatibility issue between PyTorch and the MCU used in this article, which is currently difficult to resolve. Therefore, NN, EHCNN, LOCALVIT, RESNET18, and VGG16 are not able to be applied to online SAF detection.

Tables V and VI present the online SAF detection results of different methods. In Table V, the performance of PF and nine feature extraction methods (CF_1, CF_2, CF_3, CF_4, CF_5, CF_6,

CF_7, CF_8, and CF_9) are compared. In Table VI, the performance of employed KELM and six classification methods (RF, ABT, GRBT, HiGRBT, ET, SVM) are compared.

In Table V, the online detection accuracy of PF is 99%, which is higher than that of the other eight comparison methods. Among the ten feature extraction methods in Table V, only CF_5 has a detection time exceeding 2.5 s, while the detection times of the remaining nine feature extraction methods are all within 500 ms. In Table VI, the online detection accuracy of KELM is higher than that of the other six classification methods (RF, ABT, GRBT, HiGRBT, ET). Only the detection accuracy of SVM is equal to that of KELM. In Table VI, the detection speed of classification methods can meet the requirements of the standard UL1699B.

Since the MCU is a low-power embedded processor with significantly lower computing performance than desktop-level processors in a PC, the algorithm execution time in the online experiment is higher than that in the offline experiment. In the future, this article will contemplate the utilization of high-performance embedded processors and parallel computing methods to further enhance the online detection speed.

VIII. Conclusion

In this article, SAF detection for PV systems with power electronic devices is achieved based on TFMPTF. Arc current can be decomposed into multiple modes using VMD, and those modes are transformed into two-dimensional matrixes based on TFMPTF. The singular values extracted from matrixes are input into KELM for yielding detection results.

The pivotal contribution of this article is the proposal of TFMPTF. TFMPTF is a novel methodology for analyzing the state transition characteristics of time series. TFMPTF can fully explore the dependency between adjacent data by analyzing the transition characteristics of permutation pattern states in high-dimensional space, thus more comprehensively portraying the dynamic characteristics of data compared with MTF. TFMPTF can also analyze the transition characteristics of FDE distribution states at different instants of time, overcoming the limitation of MTF that ignores the important fault information in the frequency domain.

This article has built an experimental platform that can simulate the real working environment of a PV system and has conducted research on the SAF detection method based on this experimental platform. Offline experimental results and online experimental results show that the performance of TFMPTF is significantly superior to that of traditional MTF. Under operating conditions with interference from power electronic devices, the proposed method is compared with different feature extraction methods and different classification methods. The comparison results verify the adaptability and advancement of the proposed method. Besides, online experiments demonstrate that the detection results of the proposed SAF detection method are stable, and the detection time is less than 400 ms, from which it is indicated that the real-time performance of the proposed method can satisfy the requirement of standard UL1699B and the proposed method is feasible for practical PV systems.

In future research, we plan to apply the proposed TFMPTF to various fault detection fields, such as bearing fault detection, power transformer fault detection, and air conditioning system fault detection. For different application fields, we will explore combining different time-frequency analysis methods (such as EMD, empirical wavelet transformation, local mean decomposition, etc.) with TFMPTF to enhance detection performance.

References

[1] M. Abdel-Basset, D. El-Shahat, R. K. Chakrabortty, and M. Ryan, "Parameter estimation of photovoltaic models using an improved marine predators algorithm," *Energy Convers. Manage.*, vol. 227, Oct. 2020, Art. no. 113491.

[2] N. Ong, M. A. Sadiq, and M. Said, "Fault tree analysis of fires on rooftops with photovoltaic systems," *J. Building Eng.*, vol. 46, 2022, Art. no. 103752.

[3] National Electrical Code, NFPA70, National Fire Protection Association, Batterymarch, MA, USA, 2011.

[4] Z. Yin, L. Wang, B. Zhang, L. Meng, and Y. Zhang, "An integrated DC series arc fault detection method for different operating conditions," *IEEE Trans. Ind. Electron.*, vol. 68, no. 12, pp. 12720–12729, Dec. 2021.

[5] J.-C. Gu et al., "Design of a DC series arc fault detector for photovoltaic system protection," *IEEE Trans. Ind. Appl.*, vol. 55, no. 3, pp. 2464–2471, May/Jun. 2019.

[6] M. K. Alam, F. H. Khan, J. Johnson, and J. Flicker, "PV arc-fault detection using spread spectrum time domain reflectometry (SSTDR)," in *Proc. IEEE Energy Convers. Congr. Expo.*, 2014, pp. 3294–3300.

[7] N. L. Georgijevic, M. V. Jankovic, S. Srdic, and Z. Radakovic, "The detection of series arc fault in photovoltaic systems based on the arc current entropy," *IEEE Trans. Power Electron.*, vol. 31, no. 8, pp. 5917–5930, Aug. 2016.

[8] Y. Abdullah et al., "Hurst-exponent-based detection of high-impedance DC arc events for 48-V systems in vehicles," *IEEE Trans. Power Electron.*, vol. 36, no. 4, pp. 3803–3813, Apr. 2021.

[9] Y. Liu, C. Wu, and Y. Wang, "Detection of serial arc fault on low-voltage indoor power lines by using radial basis function neural network," *Int. J. Elect. Power Energy Syst.*, vol. 83, pp. 149–157, 2016.

[10] Y. Liu et al., "Optical imaging technology application in transmission line insulator monitoring: A review," *IEEE Trans. Dielectrics Elect. Insul.*, vol. 31, no. 6, pp. 3120–3132, Dec. 2024.

[11] S. Tang, X. Diao, L. Chen, J. Zhang, and F. Yao, "Study on detection method of weak series DC fault arc in PV power generation systems," *Chin. J. Sci. Instrum.*, vol. 42, no. 03, pp. 150–160, Apr. 2021.

[12] L. Wang, H. Qiu, P. Yang, and L. Mu, "Arc fault detection algorithm based on variational mode decomposition and improved multi-scale fuzzy entropy," *Energies*, vol. 14, no. 14, Jul. 2021, Art. no. 4137.

[13] G. Zou, G. Fu, B. Han, W. Wang, and C. Liu, "Series arc fault detection based on dual filtering feature selection and improved hierarchical clustering sensitive component selection," *IEEE Sensors J.*, vol. 23, no. 6, pp. 6050–6060, Mar. 2023.

[14] V. Le, C. Miller, B.-H. Tsao, and X. Yao, "Series arc fault identification in DC distribution based on random forest predicted probability," *IEEE J. Emerg. Sel. Topics Power Electron.*, vol. 11, no. 6, pp. 5636–5648, Dec. 2023.

[15] Y. Wang, L. Hou, K. C. Paul, Y. Ban, C. Chen, and T. Zhao, "ArcNet: Series AC arc fault detection based on raw current and convolutional neural network," *IEEE Trans. Ind. Inform.*, vol. 18, no. 1, pp. 77–86, Jan. 2022.

[16] Y. Shi, H. Xu, Y. Zhang, Z. Qi, and D. Wang, "GAF-MAE: A self-supervised automatic modulation classification method based on Gramian angular field and masked autoencoder," *IEEE Trans. Cogn. Commun. Netw.*, vol. 10, no. 1, pp. 94–106, Feb. 2024.

[17] G. Niu, E. Liu, X. Wang, P. Ziehl, and B. Zhang, "Enhanced discriminate feature learning deep residual CNN for multitask bearing fault diagnosis with information fusion," *IEEE Trans. Ind. Inform.*, vol. 19, no. 1, pp. 762–770, Jan. 2023.

[18] J. Song, X. Wu, L. Qian, W. Lv, X. Wang, and S. Lu, "PMSLM eccentricity fault diagnosis based on deep feature fusion of stray magnetic field signals," *IEEE Trans. Instrum. Meas.*, vol. 73, no. 12, Dec. 2024, Art. no. 3506012.

[19] Y. Bai, J. Yang, J. Wang, Y. Zhao, and Q. Li, "Image representation of vibration signals and its application in intelligent compound fault diagnosis in railway vehicle wheelset-axlebox assemblies," *Mech. Syst. Signal Process.*, vol. 152, Nov. 2021, Art. no. 107421.

[20] F. Guo, Y. Deng, Z. Wang, J. You, and H. Gao, "Series arc fault characteristics based on gray level-gradient co-occurrence matrix," *Trans. China Electrotechnical Soc.*, vol. 33, no. 1, pp. 71–81, Jan. 2018.
[21] S. Zhang, N. Qu, T. Zheng, and C. Hu, "Series arc fault detection based on wavelet compression reconstruction data enhancement and deep residual network," *IEEE Trans. Instrum. Meas.*, vol. 71, no. 3, Mar. 2022, Art. no. 3508409.
[22] H. Gao, Z. Wang, A. Tang, C. Han, F. Guo, and B. Li, "Research on series arc fault detection and phase selection feature extraction method," *IEEE Trans. Instrum. Meas.*, vol. 70, no. 5, May 2021, Art. no. 2004508.
[23] A. Amiri, H. Samet, and T. Ghanbari, "Recurrence plots based method for detecting series arc faults in photovoltaic systems," *IEEE Trans. Ind. Electron.*, vol. 69, no. 6, pp. 6308–6315, Jun. 2022.
[24] Y. Liu, Z. Lv, S. Zhang, L. Zhang, and F. Guo, "Feature extraction and detection method of series arc faults in a motor with inverter circuits under vibration conditions," *IEEE Trans. Ind. Electron.*, vol. 71, no. 6, pp. 6294–6303, Jun. 2024.
[25] H. Gao, Z. Wang, C. Han, A. Tang, F. Guo, and B. Li, "Feature extraction method of series arc fault occurred in three-phase motor with inverter circuit," *IEEE Trans. Power Electron.*, vol. 37, no. 9, pp. 11164–11173, Sep. 2022.
[26] W. Gao, J. Hui, and G. Yang, "Series arc fault diagnosis method of photovoltaic arrays based on GASF and improved DCGAN," *Adv. Eng. Inform.*, vol. 54, Nov. 2022, Art. no. 101809.
[27] X. Zhang et al., "Fault prediction for electromechanical equipment based on spatial-temporal graph information," *IEEE Trans. Ind. Inform.*, vol. 19, no. 2, pp. 1413–1424, Feb. 2023.
[28] B. Novak, "Implementing arc detection in solar applications: Achieving compliance with the new UL 1699B Standard," Texas Instruments, Dallas, TX, USA, 2012.
[29] A. S. Campanharo, M. I. Sirer, R. D. Malmgren, F. M. Ramos, and L. A. Amaral, "Duality between time series and networks," *PLoS One*, vol. 6, no. 8, 2011, Art. no. e23378.
[30] G. Huang et al., "An insight into extreme learning machines: Random neurons, random features and kernels," *Cogn. Computation*, vol. 6, no. 3, pp. 376–390, Apr. 2014.
[31] F. Luo, G. Liu, W. Guo, G. Chen, and N. Xiong, "ML-KELM: A kernel extreme learning machine scheme for multi-label classification of real time data stream in SIoT," *IEEE Trans. Netw. Sci. Eng.*, vol. 9, no. 3, pp. 1044–1055, May/Jun. 2022.
[32] Q. Li et al., "An enhanced grey wolf optimization based feature selection wrapped kernel extreme learning machine for medical diagnosis," *Comput. Math. Methods Med.*, vol. 63, pp. 54–68, Jan. 2017.
[33] L. Li, Z. Liu, M. Tseng, and M. Lim, "Improved tunicate swarm algorithm: Solving the dynamic economic emission dispatch problems," *Appl. Soft Comput.*, vol. 108, May 2021, Art. no. 1075042021.
[34] S. Chen, Y. Meng, Z. Xie, and X. Li, "Feature selection and detection method of weak arc faults in photovoltaic systems with strong noises based on stochastic resonance," *IEEE Trans. Instrum. Meas.*, vol. 71, no. 6, Jun. 2022, Art. no. 3515213.
[35] Y. Zhang, L. Wang, Z. Yin, Y. Gao, and B. Wang, "Characteristics extraction method of aviation DC serial arc fault based on HHT," *Acta Aeronautica et Astronautica Sinica*, vol. 40, pp. 522404–522416, Jan. 2019, doi: 10.7527/S1000-6893.2018.22404.
[36] H. Abdi and L. Williams, "Principal component analysis," *Wiley Interdiscipl. Rev.: Comput. Statist.*, vol. 2, no. 4, pp. 433–459, Jul. 2010.
[37] P. Xanthopoulos, P. M. Pardalos, and T. B. Trafalis, "Linear discriminant analysis," in *Robust Data Mining*. Berlin, Germany: Springer, pp. 27–33, Jan. 2013, doi: 10.1007/978-1-4419-9878-1_4.
[38] Y.-X. Wang and Y.-J. Zhang, "Nonnegative matrix factorization: A comprehensive review," *IEEE Trans. Knowl. Data Eng.*, vol. 25, no. 6, pp. 1336–1353, Jun. 2013.
[39] J. Yan, Q. Li, and S. Duan, "A simplified current feature extraction and deployment method for DC series arc fault detection," *IEEE Trans. Ind. Electron.*, vol. 71, no. 1, pp. 625–634, Jan. 2024.
[40] H. Nhat-Duc and T. Van-Duc, "Comparison of histogram-based gradient boosting classification machine, random forest, and deep convolutional neural network for pavement raveling severity classification," *Automat. Construction*, vol. 148, Apr. 2023, Art. no. 104767.
[41] H. Shao, H. Jiang, and X. Zhang, "Intelligent fault diagnosis of aero-engine high-speed bearings using enhanced CNN," *Acta Aeronautica et Astronautica Sinica*, vol. 43, no. 09, pp. 158–171, Sep. 2022.
[42] Y. Li, K. Zhang, J. Cao, R. Timofte, and L. Van Gool, "LocalViT: Bringing locality to vision transformers," in *Proc. IEEE/RSJ Int. Conf. Intell. Robots Syst.*, Detroit, MI, USA, 2023, pp. 9598–9605.
[43] K. He, X. Zhang, S. Ren, and J. Sun, "Deep residual learning for image recognition," in *Proc. IEEE Conf. Comput. Vis. Pattern Recognit.*, 2016, pp. 770–778.
[44] Y. Zhang, W. Chan, and N. Jaitly, "Very deep convolutional networks for end-to-end speech recognition," in *Proc. IEEE Int. Conf. Acoust., Speech Signal Process.*, New Orleans, LA, USA, 2017, pp. 4845–4849.

Zhendong Yin was born in Henan, China, in 1991. He received the Ph.D. degree in electrical engineering from Nanjing University of Aeronautics and Astronautics, Nanjing, China, in 2022.

He is currently a Lecturer with the College of Electrical, Energy and Power Engineering, Yangzhou University, Yangzhou, China. His research interests include arc fault detection and machine learning.

Shuang Peng was born in Hefei, China, in 2001. She received the B.S. degree in electrical engineering and automation in 2022 from Yangzhou University, Yangzhou, China, where she is currently working toward the M.S. degree in electrical engineering.

Her research interests include the establishment of arc fault modeling and arc fault detection.

Chunyu Xiao was born in Jianhu, China, in 2001. He received the B.S. degree in electrical engineering and automation from Tianping College, Suzhou University of Science and Technology, Suzhou, China, in 2023. He is currently working toward the M.S. degree in electrical engineering with Yangzhou University, Yangzhou, China.

His research interests include arc fault detection and cable fault diagnosis.

Li Wang (Member, IEEE) received the B.E. and M.E. degrees in electrical engineering from Henan University of Science and Technology, Luoyang, China, in 1990 and 1993, respectively, and the Ph.D. degree in electrical engineering from Nanjing University of Aeronautics and Astronautics, Nanjing, China, in 2007.

She is currently a Professor with the Department of Electrical Engineering, College of Automation, Nanjing University of Aeronautics and Astronautics. Her current research interests include intelligent design, control, and protection in distribution microgrids, power electronics, solid-state breaker, fault diagnosis, prognostics and health management in power systems, power conversion and management technology, and distribution network security.

Shanshui Yang received the B.S., M.S., and Ph.D. degrees in electrical engineering from Nanjing University of Aeronautics and Astronautics, Nanjing, China, in 1991, 1994, and 2011, respectively.

He is currently an Associate Professor with the Department of Electrical Engineering, College of Automation, Nanjing University of Aeronautics and Astronautics. His current research interests include microgrid of aircraft and spacecraft, modeling and simulation, hardware-in-loop simulation, structure design, management, and control of aircraft electric systems.